scanning microscope according to the protocol of LSM510 for FRAP experiment.

2.9. Statistic analysis

The variance in a group was evaluated by use of the F-test, and the differences among the groups were evaluated by using Student's t-test.

3. Results

3.1. Temperature-dependent antifungal activity of AmBisome against S. cerevisiae

To confirm the temperature dependence of AmBisome antifungal activity, we evaluated the effect of AmBisome against S. cerevisiae at 4 or 35 °C by using the colony formation assay. As shown Fig. 1A, AmBisome showed time-dependent antifungal activity against yeast cells at 35 °C. Free AMPH-B showed stronger antifungal activity than AmBisome, and no colonies were found even after just 0.5 h of incubation with it at 35 °C. On the other hand, the antifungal effect of AmBisome was significantly reduced at 4 °C incubation (Fig. 1B), and the number of colonies was quite similar to that of the control, suggesting the antifungal effect of AmBisome to be temperature-dependent. In contrast, free AMPH-B showed strong fungicidal activity even at this temperature. These results are summarized in Fig. 1C.

3.2. Binding of AmBisome to the surface of yeast cells

In general, intact liposome is unable to pass through the fungal cell wall due to its particle size. However, the cell wall penetration of AmBisome has not been fully elucidated, and it is not clear when or where AmBisome-derived AMPH-B is transferred to the fungal cell membrane. To elucidate the mechanism, we prepared NBD-labeled AmBisome and used confocal laser-scanning microscopy to observe its localization in yeast cells after exposure. AmBisome was observed to bind to the surface of yeast cells after a 3-h exposure at 35 °C (Fig. 2A). Especially, AmBisome often bound to budding or interface site of yeast cells. Furthermore, AmBisome-derived fluorescence was observed in the cytoplasm after 24 h of incubation at this temperature (Fig. 2B). Although liposomes without encapsulated AMPH-B also bound to the cell surface, they were not incorporated into the cytoplasm after a 24-h incubation (data not shown). On the other hand, similar to the 35 °C incubation, AmBisome bound to the cell surface after a 3-h incubation at 4 °C (Fig. 2A). However, unlike that at 35 °C, AmBisome-derived fluorescence was present only on the cell surface after 24 h of incubation at the lower temperature (Fig. 2B). The cellular uptake of AmBisome after 24 h incubation at 35 °C, would be the result of permeability increase in cell membrane caused by AMPH-B transferred to the membrane, since the distribution of NBD-labeled AmBisome in S. cerevisiae in the presence of free AMPH-B at 4 °C, NBD-labeled AmBisome was observed in the cytosol (data not shown).

3.3. Temperature-dependent transfer of AMPH-B from AmBisome to yeast cells

Next, we compared the amount of AMPH-B transferred to yeast cells at different incubation temperatures. AmBisome was added to the yeast cell suspension, and the cells were incubated at 4 or 35 °C. Thereafter, the amount of AMPH-B transferred to the cells was determined by HPLC. As a result, the amount of AMPH-B in the yeast cells was reduced at 4 °C of incubation (Fig. 3), suggesting that transfer mechanism of AMPH-B from AmBisome is temperature-dependent.
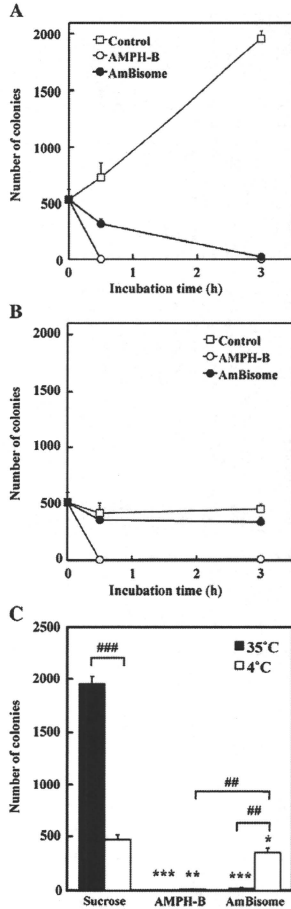

Fig. 1. Temperature-dependent antifungal activity of AmBisome against *Saccharomyces cerevisiae*. After the optical density of a S. cerevisiae suspension was adjusted to 0.1, sucrose, AMPH-B, or AmBisome (20 μM as AMPH-B) was added to the yeast cell suspension; and incubation was carried out at 35 °C (A) or 4 °C (B) for 0.5 or 3 h in MOPS-buffered RPMI 1640 medium. After the cells had been washed with PBS, they were plated on YPD/agar medium. After 24 h of incubation at 30 °C, the number of colonies formed was counted. The difference in activity between temperatures is also summarized (C). Significant differences are shown (* $P<0.05$, ** $P<0.01$, *** $P<0.001$ vs. Sucrose; ## $P<0.01$, ### $P<0.001$ as indicated by the brackets).

3.4. Disruption of AmBisome at the yeast cell surface

It is not clear whether or not the disruption of AmBisome is a prerequisite for AMPH-B release from the liposomal membrane after
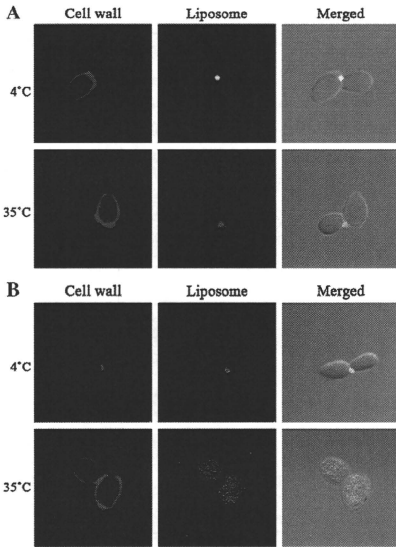
A

Cell wall	Liposome	Merged

4°C

35°C

B

Cell wall	Liposome	Merged

4°C

35°C

Fig. 2. Binding of AmBisome to cell wall of yeast cells. NBD-labeled AmBisome was added to yeast cell suspensions that were then incubated in MOPS-buffered RPMI 1640 medium at 4 or 35 °C for 3 h (A) or 24 h (B). Then, the yeast cell wall was stained with Fluorescent Brightener 28, and localization of AmBisome was observed with a confocal laser-scanning microscope. Green and blue images show AmBisome and the cell wall, respectively. Bar indicates 10 μm.

binding of AmBisome to the surface of yeast cells. To clarify this point, we prepared rhodamine-encapsulated AmBisome and investigated the disruption of the liposomes after exposure of the yeast cells to it.
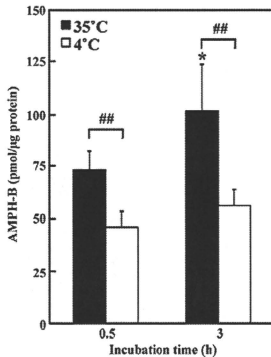

Fig. 3. Temperature-dependent transfer of AMPH-B to yeast cells. AmBisome was added to cell suspensions of *Saccharomyces cerevisiae* that were then incubated in MOPS-buffered RPMI 1640 medium at 4 or 35 °C for 0.5 or 3 h. After the cells had been washed with PBS, the amount of AMPH-B in the yeast cells was measured by HPLC. Significant differences are indicated (* P<0.05 vs. 35 °C; ## P<0.01, as indicated by the brackets).

When rhodamine-encapsulated AmBisome was incubated with yeast cells at a low density or number at 35 °C, the fluorescence of rhodamine released from AmBisome was very little, and most of the fluorescence was detected in the liposome fraction (Fig. 4A). A similar result was obtained even when the number of yeast cells was increased. Furthermore, there was no apparent difference in liposomal disruption between at 4 and 35 °C incubation (Fig. 4B). These results suggest that AmBisome was not disrupted at least until 3 h after binding to the cell surface and that AmBisome-derived AMPH-B was transferred to the fungal cell membrane without liposomal disruption.
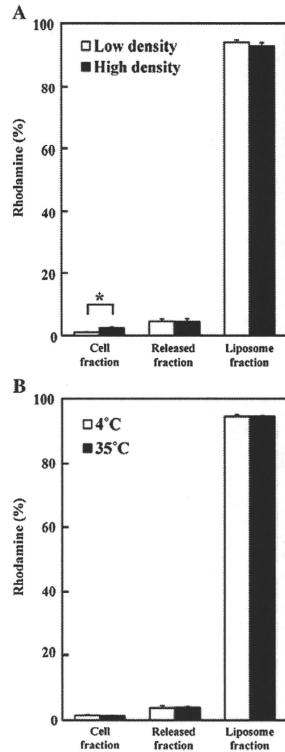
A

B

Fig. 4. Investigation of liposomal disruption during exposure of yeast cells to AmBisome. Rhodamine-encapsulating AmBisome was added to a suspension of *Saccharomyces cerevisiae* that had been adjusted to a low ($OD_{600} = 0.1$) or high ($OD_{600} = 0.3$) density, and the cells were then incubated in MOPS-buffered RPMI 1640 medium at 35 °C for 3 h (A). The culture medium was collected and ultracentrifuged to remove intact AmBisome. The fluorescence intensity of the rhodamine that had been released from rhodamine-encapsulating AmBisome into the medium was measured in the supernatant. Disruption of AmBisome at 4 °C was also examined (B). Asterisk shows a significant difference between bracketed values (* P<0.05).

A

B

C
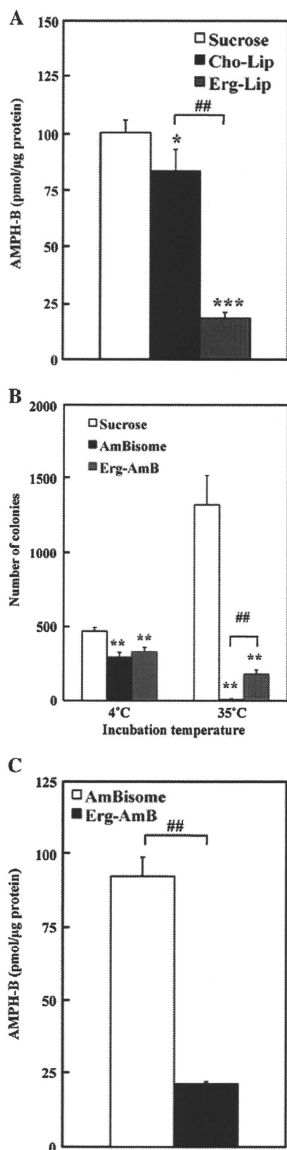
3.5. Importance of differential AMPH-B affinity for AmBisome and yeast cell membrane

To examine the importance of AMPH-B affinity for the fungal cell membrane during the transfer of AmBisome-derived AMPH-B to the membrane, we examined the transfer of AMPH-B to yeast cells in the presence of cholesterol liposomes (Cho-Lip) or ergosterol liposomes (Erg-Lip) in which AMPH-B was not entrapped. As a result, the transfer of AMPH-B from AmBisome was significantly reduced in the presence of Erg-Lip, whereas little inhibition was observed in the presence of Cho-Lip (Fig. 5A), confirming that the affinity of AMPH-B for ergosterol-containing membrane is stronger than that for cholesterol-containing one.

Next, we prepared liposomal AMPH-B containing ergosterol (Erg-AmB) instead of cholesterol and examined the antifungal activity of Erg-AmB against yeast cells. At 4 °C, the antifungal activity of Erg-AmB was attenuated just as in the case of AmBisome (Fig. 5B). However, at 35 °C Erg-AmB failed to kill all of the yeast cells whereas AmBisome completely destroyed them at this temperature (Fig. 5B). Furthermore, when the transfer of AMPH-B from Erg-AmB to the cells was investigated, the amount of AMPH-B in the cells was reduced after 3 h of incubation (Fig. 5C). These results indicate that ergosterol in the liposomes controlled the antifungal effect of liposomal AMPH-B and that the different affinity of AMPH-B for cholesterol and ergosterol played an important role in the transfer of AMPH-B to the fungal cell membrane.

3.6. Importance of liposomal membrane fluidity in temperature-dependent antifungal activity of AmBisome

Since the transfer of AMPH-B from AmBisome to the fungal cell membrane was dependent on the incubation temperature, we hypothesized that liposome membrane fluidity was a key factor in the transfer of AMPH-B. To examine the importance of membrane fluidity on the transfer of AMPH-B from AmBisome, we prepared AMPH-B liposomes composed of the highly fluid phospholipids EPC and EPG (Egg-AmB) instead of HSPC and DPPG. To measure the membrane fluidity of both liposomes, fluorescence recovery after photobleaching (FRAP) experiment was performed. NBD-labeled both liposomes were prepared, and FRAP measurement was recorded by using confocal laser scanning microscope (LSM510META). As a result, the fluorescence of NBD-PE in NBD-labeled Egg-AmB was recovered to more than 80% at 50 s after photobleaching and the diffusion coefficient was $8.2 \times 10^{-2} \mu m^2/s$, whereas the recovery of fluorescence in NBD-labeled AmBisome was little observed. This result indicates that membrane fluidity of Egg-AmB is far higher than that of AmBisome. Then, the antifungal effect of Egg-AmB against S. cerevisiae was investigated at 4 or 35 °C incubation. Egg-AmB not only completely damaged yeast cells at 35 °C, but also showed the antifungal effect at 4 °C to some extent (Fig. 6A). When localization of NBD-labeled Egg-AmB in the yeast cells was observed under the confocal laser-scanning microscope, the fluorescence of Egg-AmB was present in the cytoplasm at both 4 and 35 °C after a 3-h incubation (Fig. 6B), whereas similar images were observed only after a 24-h incubation with AmBisome at 35 °C (Fig. 2B). Furthermore, the increase in the amount

Fig. 5. Effect of ergosterol on antifungal activity of AmBisome. AmBisome was added to yeast cell suspensions of Saccharomyces cerevisiae that were then incubated in the absence or presence of drug-free cholesterol liposome (Cho-Lip) or drug-free ergosterol liposome (Erg-Lip) for 3 h at 35 °C in MOPS-buffered RPMI 1640 medium. Then, the amount of AMPH-B in the cells was measured (A). Yeast cells were also incubated with sucrose, AmBisome or liposomal AMPH-B containing ergosterol (Erg-AmB) at 4 or 35 °C for 3 h. After the cells had been washed with PBS, they were plated on YPD/agar medium. After a 24-h incubation at 30 °C, the number of formed colonies was counted (B). The amount of AMPH-B in yeast cells after 3 h of incubation at 35 °C was also measured (C). Significant differences are shown (* P<0.05, ** P<0.01, *** P<0.001 vs. Sucrose; ## P<0.01, as indicated by the bracket).

4. Discussion

It is known that liposomalization or polymerization of a drug often enables enhancement of the therapeutic effects and reduces the side effects by improving the pharmacokinetics and pharmacodynamics of the original drug in the body [15,16]. The liposomal antifungal drug AmBisome is a representative example of a liposome that incorporates AMPH-B in its membrane, enhances the stability of AMPH-B in the bloodstream and reduces the side effects of the drug [9,10]. AmBisome shows a potent antifungal effect against fungal cells such as *Candida albicans*, *Cryptococcus neoformans*, and *Aspergillus fumigatus*, resulting in the successful treatment of deep mycosis caused by them [17,18]. AmBisome exerts its effect by the binding of AMPH-B from AmBisome to ergosterol in the fungal cell membrane, which binding enhances the permeability of the fungal cell membrane and promotes the leakage of cellular substances and subsequent fungal cell death [3,19]. Thus, the transfer of AMPH-B from AmBisome to the fungal cell membrane is a key step for AmBisome to manifest its antifungal activity. In the case of other liposomal drugs, the release of the encapsulated drug from the liposome is critical for drug activity. For example, liposomal doxorubicin shows a potent cytotoxic effect against various kinds of cancer. The action mechanism of liposomal doxorubicin is considered to be as follows: Liposomal doxorubicin is incorporated into the cells by the endocytic pathway, the liposome is disrupted in lysosomes, and the encapsulated doxorubicin is released and transferred to nuclei to damage the cell. On the other hand, it is expected that the action mechanism of AmBisome against fungal cells would be different from that of other liposomal drugs against mammalian cells, since fungal cells possess a protective cell wall around their cell membrane, unlike mammalian cells [20]. In fact, it has not been fully clarified whether AmBisome can pass through the cell wall or not. In the present study, we aimed at elucidating the action mechanism of AmBisome, especially the mechanism of the transfer of AMPH-B from the liposome to ergosterol in the fungal cell membrane.

We firstly focused on the temperature dependence of AmBisome activity by comparing the antifungal effect of AmBisome against *S. cerevisiae* at 4 and 35 °C. As a result, AmBisome showed strong time-dependent antifungal activity at 35 °C, whereas free AMPH-B eradicated the yeast cells completely after just a 0.5-h incubation (Fig. 1A), indicating that AmBisome required a certain period of time to show its antifungal activity compared with AMPH-B. Furthermore, AmBisome did not show the activity at 4 °C, whereas AMPH-B showed strong activity at this same temperature (Fig. 1B, C). These results suggest that antifungal activity of AmBisome is dependent on the release and transfer of its AMPH-B to the fungal cell membrane. This temperature-dependent AmBisome activity would not be due to a difference in the localization of AmBisome in yeast cells, since AmBisome bound to yeast cells similarly at both 4 and 35 °C (Fig. 2A). Similar binding of AmBisome at 4 and 35 °C was also observed after a 0.5-h incubation (data not shown). These data also support the idea that the release and transfer of AMPH-B from AmBisome is critical for the antifungal efficacy instead of a temperature-dependent amount of AmBisome binding. In fact, the amount of AMPH-B transferred to ergosterol increased in a temperature-dependent manner (Fig. 3).

Adler-Moore et al. previously reported that gold-labeled AmBisome binds to the fungal cell wall, as observed by electron microscopy [13]. In our study, AmBisome actually bound to the cell wall and was topically observed to become localized at the budding or interface site of *S. cerevisiae* after a 3-h incubation at either 4 or 35 °C (Fig. 2A). In their review article Lesage et al. stated that the structure and components of the yeast cell wall change according to cell growth and are especially different during bud emergence and at the mother/daughter interface [21]. Thus, we hypothesize that these regions of the cell wall are susceptible to binding by AmBisome and that its
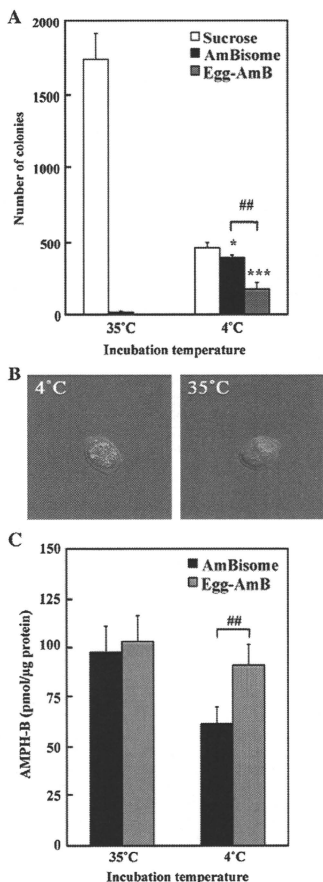
Fig. 6. Effect of liposome-membrane fluidity on antifungal activity of AmBisome. Cell suspensions of *Saccharomyces cerevisiae* were incubated with sucrose, AmBisome or liposomal AMPH-B composed of EPC and EPG (Egg-AmB) at 4 or 35 °C for 3 h in MOPS-buffered RPMI 1640 medium. After the cells had been washed with PBS, they were plated on YPD/agar medium. After 24 h of incubation at 30 °C, the number of colonies formed was counted (A). Localization of NBD-labeled Egg-AmB after a 3-h incubation at 4 or 35 °C was observed (B) and the amount of AMPH-B in the yeast cells after 3 h of incubation at 4 or 35 °C was also measured (C). Significant differences are shown (* P<0.05, *** P<0.001 vs. Sucrose; ## P<0.01, as indicated by the bracket).

of AMPH-B transferred from Egg-AmB to the cells after the 4 °C incubation was obvious (Fig. 6C). These results suggest that liposomal membrane fluidity was involved in the transfer of AMPH-B from AmBisome to the fungal cell membrane and indicate that AMPH-B in fluid liposomes would be easier to transfer to other membranes with high affinity for AMPH-B.

AMPH-B is transferred to the fungal cell membrane at these regions in a temperature-dependent manner. However, further research will be needed to elucidate whether AmBisome directly interacts with the fungal cell membrane or not.

Furthermore, AmBisome-derived fluorescence was present in the cytoplasm after 24 h of incubation at 35 °C but not at 4 °C (Fig. 2B). We speculate that the fungal cell death causes the entry of AmBisome into the cytoplasm.

We next examined the possible disruption of AmBisome for the transfer of AMPH-B to the fungal cell membrane. As a result, AmBisome-derived rhodamine release was minimal after exposure to the drug, even when the number of yeast cells was increased or the incubation temperature was changed (Fig. 4). These results indicate that the transfer of AMPH-B from AmBisome occurred at least until 3 h after attachment to the outside of fungal cells without disruption of the liposomal architecture of AmBisome.

Finally, to identify the key factor for the transfer of AMPH-B from AmBisome, we prepared liposomal AMPH-B with different lipid compositions and investigated the effect of lipid composition on AmBisome-induced antifungal activity. When AMPH-B was incorporated into liposomes containing ergosterol instead of cholesterol, the antifungal effect against *S. cerevisiae* was significantly reduced compared with that of AmBisome at 35 °C, where the membrane fluidity is considered to be similar (Fig. 5B). In addition, the amount of transferred AMPH-B to the yeast cells from Erg-AmB was decreased (Fig. 5C). It is known that the affinity of AMPH-B for ergosterol is about 10 times higher than that for cholesterol [22]. Thus, this result suggests that liposomal ergosterol prevented the release of AMPH-B from liposomes, the consequence being suppression of the transfer of AMPH-B from AmBisome to the fungal cell surface. A number of studies have been presented about the reason for the high affinity of AMPH-B to ergosterol in comparison with that to choresterol. Recently, Baran et al. suggested that AmB-ergosterol-AmB aggregates simulated to 2:1 stoichiometry retain significantly higher stability and relatively rigid, "sandwich" geometry due to Van der Waals forces and the intermolecular hydrogen bonds [23]. In contrast, cholesterol does not form this sandwich geometry that would be the reason for the low affinity of AMPH-B to cholesterol in comparison with this to ergosterol [23].

On the contrary, when AMPH-B was incorporated into liposomes composed of high-fluidity phospholipids, namely, EPC and EPG, the antifungal effect against *S. cerevisiae* was observed even at 4 °C, where the membrane fluidity is rather low and AmBisome showed little effect (Fig. 6A). In addition, the amount of AMPH-B transferred to the yeast cells from Egg-AmB was increased (Fig. 6C). When localization of NBD-labeled Egg-AmB in the yeast cells was examined, the fluorescence of Egg-AmB was present in the cytoplasm even after 0.5 h of incubation (Fig. 6B). It is known that the phase-transition temperature of EPC and HSPC is about − 10 °C and 55 °C, respectively. When the membrane fluidity of Egg-AmB and AmBisome was compared using NBD-PE by FRAP experiment, the membrane fluidity of Egg-AmB is higher than that of AmBisome. According to the result, it is reasonable that the transfer of AMPH-B from Egg-AmB to the fungal cell membrane would occur at the low temperature. Thus, these results suggest that the increased membrane fluidity enhanced the release of AMPH-B from AmBisome and stability of AMPH-B in the liposomal membrane is the key factor for the biological activity of liposomal AMPH-B.

According to the report by Legrand et al., the critical micelle concentration (CMC) of AMPH-B was 0.1 µM in aqueous solution. They showed that the concentration of free AMPH-B released by AmBisome at 1 µg/ml (1.08 µM) was about 0.08 µg/ml (0.09 µM), which was below the CMC of AMPH-B [24]. We investigated the release of AMPH-B from AmBisome at high concentration (2.22 mM) in MOPS-buffered RPMI 1640 medium at room temperature using an ultrafiltration method. As a result, time-dependent release of AMPH-B

was not observed (0.293 and 0.369 µM at 0 and 24 h after incubation, respectively; 0.013% and 0.017% of total AMPH-B in AmBisome), suggesting that AmBisome is quite stable, but allows the release of a little amount of AMPH-B (data not shown). Based on such information and results obtained in the present study, we hypothesized that ergosterol in the fungal cell membrane may be able to increase the amount of AMPH-B released from AmBisome or induce the continuous release of AMPH-B from AmBisome without direct interaction by the AmBisome after AmBisome attachment to the fungal cell wall.

5. Conclusion

Our present study demonstrated that AmBisome bound to the cell wall of yeast cells and that the AMPH-B from AmBisome was transferred to the yeast cell membrane without obvious disruption of the liposome formulation. Furthermore, we demonstrated that the transfer of AMPH-B was dependent on temperature and fluidity of the liposome membrane.

Acknowledgements

Appendix A. Supplementary data

Supplementary data associated with this article can be found, in the online version, at doi:10.1016/j.jconrel.2009.09.019.

References

[1] M.E. Klepser, E.J. Wolfe, R.N. Jones, C.H. Nightingale, M.A. Pfaller, Antifungal pharmacodynamic characteristics of fluconazole and amphotericin B tested against *Candida albicans*, Antimicrob. Agents Chemother. 41 (6) (1997) 1392–1395.
[2] L. Ostrosky-Zeichner, K.A. Marr, J.H. Rex, S.H. Cohen, Amphotericin B: time for a new "gold standard", Clin. Infect. Dis. 37 (3) (2003) 415–425.
[3] B.E. Cohen, Concentration- and time-dependence of amphotericin-B induced permeability changes across ergosterol-containing liposomes, Biochim. Biophys. Acta 857 (1) (1986) 117–122.
[4] I. Fournier, J. Barwicz, P. Tancrede, The structuring effects of amphotericin B on pure and ergosterol- or cholesterol-containing dipalmitoylphosphatidylcholine bilayers: a differential scanning calorimetry study, Biochim. Biophys. Acta 1373 (1) (1998) 76–86.
[5] K.M. Wasan, G. Lopez-Berestein, The interaction of liposomal amphotericin B and serum lipoproteins within the biological milieu, J. Drug Target 2 (5) (1994) 373–380.
[6] R. Sabra, R.A. Branch, Amphotericin B nephrotoxicity, Drug Saf 5 (2) (1990) 94–108.
[7] I. Bekersky, R.M. Fielding, D.E. Dressler, J.W. Lee, D.N. Buell, T.J. Walsh, Plasma protein binding of amphotericin B and pharmacokinetics of bound versus unbound amphotericin B after administration of intravenous liposomal amphotericin B (AmBisome) and amphotericin B deoxycholate, Antimicrob. Agents Chemother. 46 (3) (2002) 834–840.
[8] J. Adler-Moore, R.T. Proffitt, Effect of tissue penetration on AmBisome efficacy, Curr. Opin. Investig. Drugs 4 (2) (2003) 179–185.
[9] K. Takemoto, Y. Yamamoto, Y. Ueda, Evaluation of antifungal pharmacodynamic characteristics of AmBisome against *Candida albicans*, Microbiol. Immunol. 50 (8) (2006) 579–586.
[10] K. Takemoto, Y. Yamamoto, Y. Ueda, Y. Sumita, K. Yoshida, Y. Niki, Comparative study on the efficacy of AmBisome and Fungizone in a mouse model of pulmonary aspergillosis, J. Antimicrob. Chemother. 57 (4) (2006) 724–731.
[11] E. Briones, C.I. Colino, J.M. Lanao, Delivery systems to increase the selectivity of antibiotics in phagocytic cells, J. Control Release 125 (3) (2008) 210–227.
[12] J. Adler-Moore, AmBisome targeting to fungal infections, Bone Marrow Transplant. 14 (Suppl 5) (1994) S3–7.
[13] J. Adler-Moore, R.T. Proffitt, AmBisome: liposomal formulation, structure, mechanism of action and pre-clinical experience, J. Antimicrob. Chemother. 49 (Suppl 1) (2002) 21–30.
[14] V.J. Cid, A. Duran, F. del Rey, M.P. Snyder, C. Nombela, M. Sanchez, Molecular basis of cell integrity and morphogenesis in *Saccharomyces cerevisiae*, Microbiol. Rev. 59 (3) (1995) 345–386.
[15] T.M. Allen, P.R. Cullis, Drug delivery systems: entering the mainstream, Science 303 (5665) (2004) 1818–1822.
[16] G. Gaucher, M.H. Dufresne, V.P. Sant, N. Kang, D. Maysinger, J.C. Leroux, Block copolymer micelles: preparation, characterization and application in drug delivery, J. Control Release 109 (1–3) (2005) 169–188.

[17] J.P. Adler-Moore, S.M. Chiang, A. Satorius, D. Guerra, B. McAndrews, E.J. McManus, R.T. Proffitt, Treatment of murine candidosis and cryptococcosis with a unilamellar liposomal amphotericin B formulation (AmBisome), J. Antimicrob. Chemother 28 (Suppl B) (1991) 63–71.

[18] A.C. Leenders, P. Reiss, P. Portegies, K. Clezy, W.C. Hop, J. Hoy, J.C. Borleffs, T. Allworth, R.H. Kauffmann, P. Jones, F.P. Kroon, H.A. Verbrugh, S. de Marie, Liposomal amphotericin B (AmBisome) compared with amphotericin B both followed by oral fluconazole in the treatment of AIDS-associated cryptococcal meningitis, AIDS 11 (12) (1997) 1463–1471.

[19] M. Baginski, H. Resat, E. Borowski, Comparative molecular dynamics simulations of amphotericin B-cholesterol/ergosterol membrane channels, Biochim. Biophys. Acta 1567 (1–2) (2002) 63–78.

[20] M. Kirkham, R.G. Parton, Clathrin-independent endocytosis: new insights into caveolae and non-caveolar lipid raft carriers, Biochim. Biophys. Acta 1745 (3) (2005) 273–286.

[21] G. Lesage, H. Bussey, Cell wall assembly in *Saccharomyces cerevisiae*, Microbiol. Mol. Biol. Rev. 70 (2) (2006) 317–343.

[22] J.D. Readio, R. Bittman, Equilibrium binding of amphotericin B and its methyl ester and borate complex to sterols, Biochim. Biophys. Acta 685 (2) (1982) 219–224.

[23] M. Baran, E. Borowski, J. Mazerski, Molecular modeling of amphotericin B-ergosterol primary complex in water II, Biophys. Chem. 141 (2–3) (2009) 162–168.

[24] P. Legrand, M. Cheron, L. Leroy, J. Bolard, Release of amphotericin B from delivery systems and its action against fungal and mammalian cells, J. Drug Target 4 (5) (1997) 311–319.

A novel DDS strategy, "dual-targeting", and its application for antineovascular therapy

Yuki Murase [a], Tomohiro Asai [a], Yasufumi Katanasaka [a], Tomoki Sugiyama [a], Kosuke Shimizu [a], Noriyuki Maeda [b], Naoto Oku [a,*]

[a] Department of Medical Biochemistry and Global COE Program, Graduate School of Pharmaceutical Sciences, University of Shizuoka, 52-1 Yada, Suruga-ku, Shizuoka 422-8526, Japan
[b] Nippon Fine Chemical Co. Ltd., Takasago, Hyogo 676-0074, Japan

ABSTRACT

Dual-targeting liposomes modified with Ala-Pro-Arg-Pro-Gly (APRPG) and Gly-Asn-Gly-Arg-Gly (GNGRG) peptides were developed. They remarkably associated to growing human umbilical vein endothelial cells (HUVECs) compared with single-targeting liposomes modified with APRPG or GNGRG. Doxorubicin (DOX) encapsulated in the dual-targeting liposomes significantly suppressed the growth of HUVECs compared with that in single-targeting liposomes. The dual-targeting liposomes containing DOX strongly suppressed tumor growth in Colon26 NL-17 carcinoma-bearing mice. Confocal microscopic data indicated that this anticancer effect was brought by the association of these liposomes to angiogenic vessels in the tumor. These findings suggest that "dual-targeting" would be a hopeful method for targeting therapies.

© 2009 Elsevier Ireland Ltd. All rights reserved.

1. Introduction

Liposomes are known as one of the most effective drug carriers for cancer therapy. In liposomal DDS technologies, polyethylene glycol (PEG)-modified liposomes are well known as useful drug carriers for cancer therapy. PEG-

modified liposomes have long-circulating characteristics through avoidance of trapping by a reticuloendothelial system (RES) such as liver and spleen [1,2]. PEG-modified liposomes tend to accumulate in tumor tissues thorough passive targeting since leaky angiogenic vessels brings enhanced permeability and retention (EPR) effect [3,4]. In fact, PEG-modified liposomes containing doxorubicin (DOX) have been used in clinical cancer therapy. On the other hand, active-targeting using liposomes modified with ligands such as antibodies and peptides achieves more selective drug delivery to tumor tissues. These ligands that recognize tumor-associated molecules are conjugated to the head of PEG-chain of liposomes [5,6]. Active-targeting using ligand-modified long-circulating PEG-liposomes would be more effective since these liposomes have great opportunity to meet target tissues during long circulation time. Indeed, cancer treatments with stealth immunoliposomes and transferrin-conjugated PEG-liposomes have been successful in animal models [7–9].

Angiogenesis is a critical event for growth and hematogenous metastasis of tumors [10,11]. Therefore, antiangiogenic therapies are promised to suppress both tumor growth and metastasis [12,13]. Antineovascular therapy (ANET), one of antiangiogenic therapies, causes indirect tumor regression through damaging angiogenic vessels, which is achieved by delivering anticancer drugs to them with DDS technologies such as liposomes [14]. ANET could avoid the acquirement of drug resistance resulting from genetic or epigenetic mutation since this therapy targets angiogenic endothelial cells that are genetically stable [13]. The therapeutic effect of anticancer drugs would be amplified by targeting angiogenic cells since a large number of cancer cells are maintained by a relatively few endothelial cells for their survival and growth [15]. Furthermore, ANET is expected to have a broad anticancer spectrum since angiogenic vessels are necessary for all kinds of solid tumors.

We previously performed in vivo biopanning of a phage-displayed peptide library using an angiogenesis mouse model to identify a targeting-ligand for angiogenic vessel-specific drug delivery. As a result, Ala-Pro-Arg-Pro-Gly (APRPG) was identified as a novel peptide homing to angiogenic vessels [14,16]. Arap and coworkers injected phage-displayed peptide library into the circulation of human breast carcinoma-bearing mice and identified Asn-Gly-Arg (NGR) and Arg-Gly-Asp (RGD) motif [17]. NGR and RGD peptides motif bind selectively to CD13 (aminopeptidase N) and $\alpha_v\beta_3$ or $\alpha_v\beta_5$ integrins, respectively [18–20]. These peptides such as PRP, NGR and RGD were useful as targeting-ligands of liposomes since modification of liposomes with each of these peptides enhanced anticancer activity of DOX in tumor-bearing mice [21,22]. Until now, these peptides were used for angiogenic vessel-targeting individually and combinational effect of them has not been investigated. In the present study, we proposed a novel active-targeting strategy named "dual-targeting" in which two different kinds of targeting-ligands are modified on drug carriers. We hypothesized that two different ligands on the surface of liposomes might enable to enhance potential of active-targeting cooperatively. We prepared dual-targeting liposomes modified with both APRPG and GNGRG and investigated the usefulness of them for ANET.

2. Materials and methods

2.1. Preparation of liposomes

All lipids were the products of Nippon Fine Chemical, Co. Ltd. (Takasago, Hyogo, Japan). Distearoylphosphatidylcholine (DSPC) and cholesterol with DSPE-PEG, DSPE-PEG-APRPG or DSPE-PEG-GNGRG (10:5:1 as a molar ratio), or with DSPE-PEG-APRPG and DSPE-PEG-GNGRG (10:5:0.5:0.5 as a molar ratio) were dissolved in chloroform/methanol, dried under reduced pressure, and stored in vacuo for at least 1 h. Liposomes were prepared by hydration of the thin lipid film with PBS, and frozen and thawed for three cycles using liquid nitrogen. Then, the liposomes were sized by extruding thrice through a polycarbonate membrane filter with 100 nm pores. Particle size and ζ-potential of the liposomes diluted

with PBS were measured by use of a Zetasizer Nano ZS (MALVERN, Worcestershire UK, USA).

For an association study and a histochemical analysis, DiIC$_{18}$ (Molecular Probes Inc., Eugene, OR, USA) was added to the initial chloroform/methanol solution at a dose of 5 mol% of DSPC. For a biodistribution study, a trace amount of [^{3}H]cholesteryl hexadecyl ether (GE Healthcare UK Ltd., Buckinghamshire, England) was added to the initial solution. For a cell proliferation assay and a therapeutic experiment, DOX-encapsulated liposomes were prepared by a modification of the remote-loading method as described previously [23]. The encapsulation efficiency of DOX into the liposomes was more than 90% throughout the experiment. The concentration of DOX was determined by an absorbance at 484 nm.

2.2. Association of liposomes to HUVECs

Human umbilical vein endothelial cells (HUVECs, 2×10^4 cells/well) were seeded on gelatin-coated 24-well plate and cultured in endothelial cell growth medium-2 (EGM-2, Cambrex Bio Science Walkersville, Walkersville, MD) for 48 h at 37 °C in a 5% CO$_2$ incubator. Then, DiIC$_{18}$-labeled liposomes were added (final 0.05 or 0.1 mM as DSPC concentration) and incubated for 4 h at 37 °C. After washing these cells with ice-cold PBS, they were solubilized in 0.1% sodiumdodecylsulfate-containing 10 mM Tris buffer (pH 7.4). The amount of DiIC$_{18}$-labeled liposomes transferred to HUVECs was fluorometrically determined at an excitation wavelength of 549 nm and an emission wavelength of 592 nm by Infinite M200 (Tecan, Grödig, Austria). The amount of proteins in the samples was determined by bicinchoninic acid (BCA) protein assay (Pierce Chemical, IL). The amount of liposomes transferred into HUVECs was corrected by the amount of cellular proteins.

2.3. Cell proliferation assay

HUVECs (5×10^3 cells/well) were seeded on gelatin-coated 96-well plate and cultured in EGM-2 overnight at 37 °C in a 5% CO$_2$ incubator. Then, DOX or DOX-encapsulated liposomes were added (final 10 μg/ml as a dose of DOX) and incubated for 30 min at 37 °C. After washing these cells with PBS, they were cultured in EGM-2 for 48 h. Then, the growth of these cells was evaluated by a modified MTT assay using TetraColor One^{TM} (Seikagaku, Tokyo, Japan).

2.4. Biodistribution study

Colon26 NL-17 cells were cultured in DME/Ham's F12 medium (WAKO, Osaka, Japan) supplemented with streptomycin (100 μg/ml), penicillin (100 units/ml), and 10% fetal bovine serum (FBS) at 37 °C in 5% CO$_2$. After harvesting of these cells, 1.0×10^6 cells were implanted subcutaneously into the posterior flank of 4-week-old BALB/c male mice (Japan SLC Inc., Shizuoka, Japan). The biodistribution study was performed at day 11 after tumor implantation. Size-matched Colon26 NL-17-bearing mice ($n = 5$) were injected with the radiolabeled liposomes via a tail vein (74 kBq/mouse). Twenty-four hours after the injection, the mice

were sacrificed under deep anesthesia for collection of the blood. The plasma was obtained by centrifugation (600g for 5 min). Then the heart, lung, liver, spleen, kidney and tumor were removed, washed with saline, and weighed. The radioactivity in each organ was determined with a liquid scintillation counter (Aloka LSC-3100). Distribution data are presented as % dose per 100 mg tissue. The total amount in the plasma was calculated based on the body weight of mice, where the plasma volume was assumed to be 4.27% of the body weight based on the data of total blood volume [23]. The animals were cared for according to the animal facility guidelines of the University of Shizuoka.

2.5. Intratumoral localization of liposomes

Colon26 NL-17 cells (1.0×10^6 cells/mouse) were inoculated as described above. DiI-labeled liposomes were administered via a tail vein of the mice at 10 days after tumor implantation. At 3 h after injection of the liposomes, the mice were sacrificed under deep anesthesia, and the tumors were dissected. The tumor tissues were embedded in optimal cutting temperature compound (Sakura Finetech, Co. Ltd., Tokyo, Japan) and frozen at −80 °C. Tumor sections (10 μm) were prepared with cryostat microtome (HM 505E, Microm, Walldorf, Germany), mounted on MAS-coated slides (Matsunami Glass Ind., Ltd., Japan), air-dried for 1 h, and washed twice with PBS. Endogenous avidin activity was blocked with a blocking reagent kit (Vector Laboratories, CA). After these sections had been blocked with 1% BSA in PBS, they were incubated with biotinylated anti-mouse CD31 rat monoclonal antibody (Becton Dickinson Lab., Franklin Lakes, NJ) for 18 h at 4 °C and then visualized after incubation with streptavidin-Alexa fluor 488 conjugates (Molecular Probes Inc., Eugene, OR) for 30 min at room temperature in a humid chamber. Then, the sections were mounted with Perma Fluor Aqueous Mounting Medium (Thermo Shandon, PA) and fluorescently observed with the LSM 510 META confocal microscope (Carl Zeiss, Co. Ltd., Germany).

2.6. Therapeutic experiment

Colon26 NL-17 cells (1.0×10^6 cells/mouse) were inoculated as described above. DOX-encapsulated liposomes or PBS were administered intravenously into the tumor-bearing mice ($n = 5$) at day 8, 11, 14 and 17 after the tumor inoculation. The treatment was started when the tumor volumes had reached about 0.1 cm^3. The injected dose of DOX in each administration was 3 mg/kg (about 0.05 mmol/kg as a dose of DSPC in liposomal formulations). The size of the tumors and the body weight of each mouse were monitored. Two bisecting diameters of each tumor were measured with slide calipers to determine the tumor volume. Calculation of the tumor volume was performed using the formula $0.4 \times (a \times b^2)$, where a is the largest and b is the smallest diameter.

2.7. Statistical analysis

Differences in a group were evaluated by an analysis of variance (ANOVA) with the Tukey post hoc test.

3. Results

3.1. Characteristics of dual-targeting liposomes

Particle size and ζ-potential of liposomes were determined. All kinds of liposomes used in the following experiments had the size of 110–150 nm in diameter and slightly negative charges (Table 1).

3.2. Affinity of dual-targeting liposomes to proliferative endothelial cells

To investigate whether dual-targeting liposomes (Dual-PEG-Lip) have more potent affinity to angiogenic vessels compared with APRPG-PEG-modified or GNGRG-PEG-modified single-targeting liposomes (PRP-PEG-Lip or NGR-PEG-Lip), the association of dual-targeting liposomes to HUVECs stimulated with proangiogenic cytokines were determined (Fig. 1). As a result, all liposomes modified with targeting-peptides were significantly associated to HUVECs compared with PEG-modified liposomes (PEG-Lip) in a dose dependent manner. Moreover, the association amount of Dual-PEG-Lip to HUVECs was significantly higher than that of PRP-PEG-Lip and NGR-PEG-Lip.

3.3. Effect of DOX encapsulated in dual-targeting liposomes on the growth of HUVECs

Anti-proliferative effect of DOX encapsulated in dual-targeting liposomes (Dual-PEG-DOX) on HUVECs was determined (Fig. 2). DOX encapsulated in all targeting-liposomes tested (PRP-PEG-Lip containing DOX, PRP-PEG-DOX; NGR-PEG-Lip containing DOX, NGR-PEG-DOX; and Dual-

Table 1
Particle size and ζ-potential of liposomes.

	Particle size (nm)	ζ-Potential (mV)
PEG-Lip	121.6 ± 11.7	−3.1 ± 0.9
PRP-PEG-Lip	124.8 ± 21.4	−3.1 ± 0.6
NGR-PEG-Lip	122.7 ± 22.4	−2.3 ± 0.9
Dual-PEG-Lip	116.2 ± 9.7	−2.9 ± 0.8
PEG-DOX	145.7 ± 16.2	−1.2 ± 0.6
PRP-PEG-DOX	143.7 ± 28.4	−2.0 ± 0.3
NGR-PEG-DOX	145.0 ± 44.4	−2.0 ± 0.3
Dual-PEG-DOX	136.7 ± 34.0	−2.8 ± 1.6

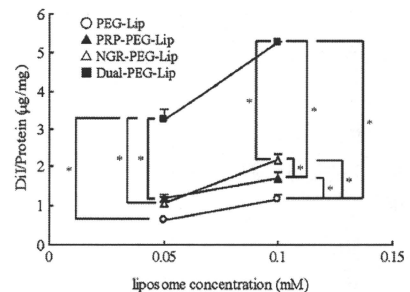Parameters represent the mean ± SD.

Fig. 1. The association of Dual-PEG-Lip to proliferating HUVECs. HUVECs were cultured in EGM-2 for 48 h, then added the indicated dose of DiIC$_{18}$-labeled liposomes and incubated for 4 h at 37 °C. After washing, the amount of liposomes associated to HUVECs was determined fluorometrically. Liposomes associated to HUVECs were represented as amount of DiIC$_{18}$ per cellular protein amount. Open circles, PEG-Lip; closed triangles, PRP-PEG-Lip; open triangles, NGR-PEG-Lip; and closed squares, Dual-PEG-Lip. Data show the mean value and SD. Significant differences are shown with asterisks ($^*P < 0.01$).
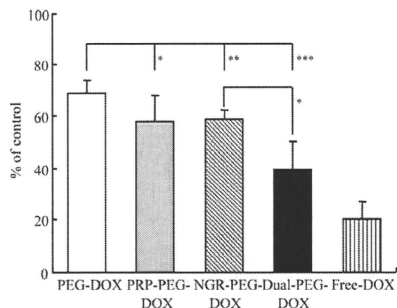
Fig. 2. Anti-proliferative effect of Dual-PEG-DOX on proliferating HUVECs. HUVECs were cultured in EGM-2 overnight. Then, DOX or DOX encapsulated in the liposomes were added (final concentration of 10 μg/ml as a DOX dosage) and incubated for 30 min at 37 °C. After 48 h incubation, cell growth was determined by modified MTT assay using TetraColor One™. Data represent the anti-proliferative effects of each sample as percent of control and SD. Open bar, PEG-DOX; grey bar, PRP-PEG-DOX; hatched bar, NGR-PEG-DOX; closed bar, Dual-PEG-DOX; and stripe bar, Free-DOX. Asterisks indicate the significant differences: $^*P < 0.05$, $^{**}P < 0.01$ and $^{***}P < 0.001$.

PEG-DOX) significantly suppressed the growth of HUVECs compared with DOX encapsulated in PEG-Lip (PEG-DOX). Furthermore, the antiproliferative effect of Dual-PEG-DOX was significantly higher than that of NGR-PEG-DOX and tended to be high compared with that of PRP-PEG-DOX. These anti-proliferative effects were observed in a dose dependent manner (Supplemental data).

3.4. Biodistribution of dual-targeting liposomes

The biodistribution of the liposomes was determined in Colon26 NL-17 carcinoma-bearing mice (Fig. 3). NGR-PEG-Lip tended to accumulate in the spleen. In contrast, the accumulation of PRP-PEG-Lip in the spleen
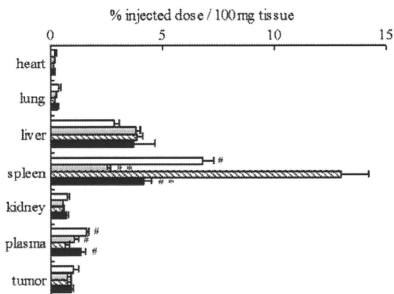

Fig. 3. Biodistribution of Dual-PEG-Lip in the tumor-bearing mice. Size-matched Colon26 NL-17-bearing mice ($n = 5$) were injected with radio-labeled liposomes via a tail vein. Twenty-four hours after injection, the radioactivity in each organ was determined. Data are presented as percent of the injected dose per 100 mg tissue and SD. Open bar, PEG-Lip; grey bar, PRP-PEG-Lip; hatched bar, NGR-PEG-Lip; and closed bar, Dual-PEG-Lip. Significant differences are shown with asterisks (versus PEG-Lip): $^*P < 0.01$, and sharps (versus NGR-PEG-Lip): $^\#P < 0.01$.

was lower than PEG-Lip. Interestingly, Dual-PEG-Lip did not accumulate in the spleen although it contains a half amount of GNGRG peptides in comparison to NGR-PEG-Lip. The amount of NGR-PEG-Lip in the plasma was significantly lower than other liposomes tested. On the other hand, Dual-PEG-Lip showed a long-circulating property like PEG-Lip and PRP-PEG-Lip. The accumulation in the tumor was similar level among all liposomes tested.

3.5. Intratumoral localization of dual-targeting liposomes

Intratumoral localization of the liposomes was determined in the tumor syngrafts to evaluate the affinity of Dual-PEG-Lip to angiogenic vessels in vivo (Fig. 4). As shown in Fig. 4a–c, PEG-Lip was observed around tumor angiogenic vessels, indicating that it extravasated from these vessels. On the other hand, PRP-PEG-Lip (Fig. 4d–f), NGR-PEG-Lip (Fig. 4g–i) and Dual-PEG-Lip (Fig. 4j–l) localized on angiogenic vessels. In addition, Dual-PEG-Lip localized on angiogenic vessels more intensely than PRP-PEG-Lip and NGR-PEG-Lip.

3.6. Therapeutic effect of DOX encapsulated in dual-targeting liposomes

The therapeutic effect of Dual-PEG-DOX against the solid tumor was examined (Fig. 5). The body weight change was not observed in all groups tested (data not shown). As shown in the figure, significant differences in the tumor volume were observed between liposomal DOX-treated group (PEG-DOX, PRP-PEG-DOX, NGR-PEG-DOX or Dual-PEG-DOX) and control group 24 days after tumor implantation. Antitumor effect of Dual-PEG-DOX was the highest among all liposomal formulations. Dual-PEG-DOX significantly suppressed the tumor growth in comparison to PEG-DOX.

4. Discussion

In the present study, we proposed a novel targeting strategy, "dual-targeting", and applied it to ANET. We firstly determined the affinity of liposomes modified with two different targeting peptides (namely APRPG and GNGRG) to proliferating HUVECs as an in vitro model of angiogenic endothelial cells. As a result, Dual-PEG-Lip showed the highest affinity to proliferating HUVECs dose-dependently. This data suggests that two different kinds of angiogenic vessel-targeting peptides on the liposomal surface cooperatively enhanced the association of these liposomes to proliferating HUVECs. Saul et al. previously reported that liposomes targeting epidermal growth factor receptors (EGFR) and folate receptors (FR) improved selectivity to target cells compared with single-ligand liposomes [24]. Although these liposomes attenuated non-specific binding to non-target cells, the affinity of them to target cells was not determined. In contrast, our data provided the evidence that dual-targeting achieved enhancement of the targeting activity. In fact, Dual-PEG-DOX suppressed the growth of proliferating HUVECs in comparison to non-targeting or single-targeting liposomal DOX, reflecting that Dual-PEG-Lip showed the highest affinity to proliferating HUVECs.

Previous study showed that liposomes modified with NGR accumulated in the spleen after intravenous injection [22]. Our data also indicated that NGR-PEG-Lip tended to accumulate in the spleen. However, this wrong property caused by NGR was improved in Dual-PEG-Lip administration group. Consequently, Dual-PEG-Lip remained in the plasma more than NGR-PEG-Lip. These results might be related to the amount of peptide on the liposome surface although precise mechanism is not cleared at present. There were no statistical differences in the accumulation
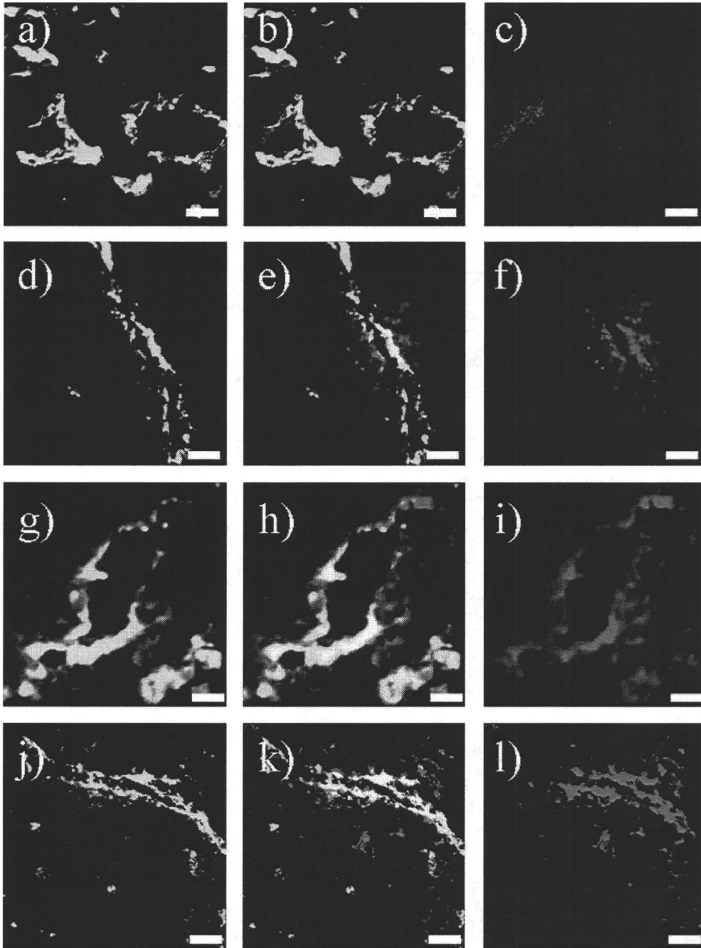
Fig. 4. Localization of Dual-PEG-Lip in the tumor. Colon26 NL-17-bearing mice were intravenously injected with PEG-Lip (a–c), PRP-PEG-Lip (d–f), NGR-PEG-Lip (g–i) or Dual-PEG-Lip (j–l) labeled with DiIC$_{18}$ at day 10 after tumor implantation. At 3 h after injection, the tumors were dissected, and then frozen-sections (10 μm) were prepared. Immunofluorescence staining for CD31 was performed to visualize endothelial cells. Green images indicate CD31-positive regions (a, d, g and j), and red images show liposomal distribution (c, f, i and l). Panels b, e, h and k represent the merged images of them. Yellow portions indicate the localization of liposomes at the site of vascular endothelial cells. Scale bars represent 20 μm.

of liposomes to tumor tissue. However, intratumoral distribution of Dual-PEG-Lip in Colon26 NL-17-bearing mice was obviously different. The results showed that targeting liposomes bound to angiogenic vessels whereas PEG-Lip did not. Moreover, Dual-PEG-Lip showed further enhanced targeting activity to angiogenic vessels in comparison to PRP-PEG-Lip or NGR-PEG-Lip along with the result from the in vitro association experiment. Thus, the association
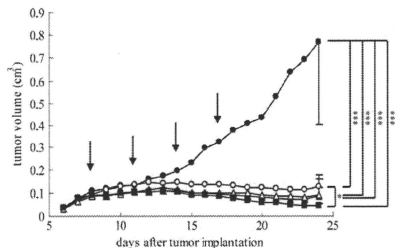
Fig. 5. Therapeutic effect of Dual-PEG-DOX in tumor-bearing mice. Colon26 NL-17-bearing mice ($n = 5$) were intravenously injected with PBS (closed circles), PEG-DOX (open circles), PRP-PEG-DOX (closed triangles), NGR-PEG-DOX (open triangles) or Dual-PEG-DOX (closed squares) at days 8, 11, 14 and 17 after tumor implantation. Injected dose of liposomal DOX were 3 mg/kg as DOX in each administration. Tumor volume and body weight (data not shown) of tumor-bearing mice were monitored. Data represent the mean tumor volume and SD, where the SD bars are shown only for the last points (day 24). Arrows show the days of injection. Asterisks show the significant differences: $^*P < 0.05$ and $^{***}P < 0.001$.

with angiogenic vessels *in vivo* was also improved effectively by use of dual-targeting liposomes. In our previous studies, we demonstrated that DOX encapsulated in angiogenic vessel-targeted liposomes was localized exclusively to angiogenic endothelial cells and damaged them [25]. Finally the therapeutic effect of Dual-PEG-DOX against the solid tumor was examined. Our data showed that Dual-PEG-DOX strongly suppressed the tumor growth compared with other formulations due to their potent targeting ability to angiogenic vessels. The therapeutic effects of Dual-PEG-DOX might be further enhanced by adjusting the amount of DOX in the liposomes. These findings give enough evidences for usefulness of dual-targeting liposomes in ANET.

From the result obtained in this study, it would be expected that "dual-targeting" is a useful targeting strategy for ANET. For example, combination of peptides used here and RGD would be promising approach. In addition, the investigation about the rate of peptides on dual-targeting liposomal surface would be interesting since we modified an equal amount of APRPG and GNGRG as a tentative rate. The most notable finding presented here is the fact that targeting ability of liposomes was enhanced by dual-targeting. Dual-targeting would be available for a number of targeting therapies because most of target organs express multiple address molecules.

Conflicts of interest

None declared.

Acknowledgement

Appendix A. Supplementary material

Supplementary data associated with this article can be found, in the online version, at doi:10.1016/j.canlet.2009.06.008.

References

[1] T. Sakakibara, F.A. Chen, H. Kida, K. Kunieda, R.E. Cuenca, F.J. Martin, R.B. Bankert, Doxorubicin encapsulated in sterically stabilized liposomes is superior to free drug or drug-containing conventional liposomes at suppressing growth and metastases of human lung tumor xenografts, Cancer Res. 56 (1996) 3743–3746.

[2] D.D. Lasic, Doxorubicin in sterically stabilized liposomes, Nature 380 (1996) 561–562.

[3] Y. Matsumura, H. Maeda, A new concept for macromolecular therapeutics in cancer chemotherapy: mechanism of tumoritropic accumulation of proteins and the antitumor agent smancs, Cancer Res. 46 (1986) 6387–6392.

[4] F.M. Muggia, Doxorubicin-polymer conjugates: further demonstration of the concept of enhanced permeability and retention, Clin. Cancer Res. 5 (1999) 7–8.

[5] J.W. Park, K. Hong, D.B. Kirpotin, O. Meyer, D. Papahadjopoulos, C.C. Benz, Anti-HER2 immunoliposomes for targeted therapy of human tumors, Cancer Lett. 118 (1997) 153–160.

[6] X.B. Xiong, Y. Huang, W.L. Lu, X. Zhang, H. Zhang, T. Nagai, Q. Zhang, Intracellular delivery of doxorubicin with RGD-modified sterically stabilized liposomes for an improved antitumor efficacy: in vitro and in vivo, J. Pharm. Sci. 94 (2005) 1782–1793.

[7] C. Brignole, D. Marimpietri, C. Gambini, T.M. Allen, M. Ponzoni, F. Pastorino, Development of Fab' fragments of anti-GD(2) immunoliposomes entrapping doxorubicin for experimental therapy of human neuroblastoma, Cancer Lett. 197 (2003) 199–204.

[8] F. Pastorino, C. Brignole, D. Marimpietri, P. Sapra, E.H. Moase, T.M. Allen, M. Ponzoni, Doxorubicin-loaded Fab' fragments of anti-disialoganglioside immunoliposomes selectively inhibit the growth and dissemination of human neuroblastoma in nude mice, Cancer Res. 63 (2003) 86–92.

[9] O. Ishida, K. Maruyama, H. Tanahashi, M. Iwatsuru, K. Sasaki, M. Eriguchi, H. Yanagie, Liposomes bearing polyethyleneglycol-coupled transferrin with intracellular targeting property to the solid tumors in vivo, Pharm. Res. 18 (2001) 1042–1048.

[10] J. Folkman, P.A. D'Amore, Blood vessel formation: what is its molecular basis?, Cell 87 (1996) 1153–1155.

[11] M.S. O'Reilly, L. Holmgren, C. Chen, J. Folkman, Angiostatin induces and sustains dormancy of human primary tumors in mice, Nat. Med. 2 (1996) 689–692.

[12] M. Skobe, P. Rockwell, N. Goldstein, S. Vosseler, N.E. Fusenig, Halting angiogenesis suppresses carcinoma cell invasion, Nat. Med. 3 (1997) 1222–1227.

[13] T. Browder, C.E. Butterfield, B.M. Kraling, B. Shi, B. Marshall, M.S. O'Reilly, J. Folkman, Antiangiogenic scheduling of chemotherapy improves efficacy against experimental drug-resistant cancer, Cancer Res. 60 (2000) 1878–1886.

[14] N. Oku, T. Asai, K. Watanabe, K. Kuromi, M. Nagatsuka, K. Kurohane, H. Kikkawa, K. Ogino, M. Tanaka, D. Ishikawa, H. Tsukada, M. Momose, J. Nakayama, T. Taki, Anti-neovascular therapy using novel peptides homing to angiogenic vessels, Oncogene 21 (2002) 2662–2669.

[15] R.K. Jain, Normalizing tumor vasculature with anti-angiogenic therapy: a new paradigm for combination therapy, Nat. Med. 7 (2001) 987–989.

[16] T. Asai, K. Shimizu, M. Kondo, K. Kuromi, K. Watanabe, K. Ogino, T. Taki, S. Shuto, A. Matsuda, N. Oku, Anti-neovascular therapy by liposomal DPP-CNDAC targeted to angiogenic vessels, FEBS Lett. 520 (2002) 167–170.

[17] W. Arap, R. Pasqualini, E. Ruoslahti, Cancer treatment by targeted drug delivery to tumor vasculature in a mouse model, Science 279 (1998) 377–380.

[18] R. Pasqualini, E. Koivunen, R. Kain, J. Lahdenranta, M. Sakamoto, A. Stryhn, R.A. Ashmun, L.H. Shapiro, W. Arap, E. Ruoslahti, Aminopeptidase N is a receptor for tumor-homing peptides and a target for inhibiting angiogenesis, Cancer Res. 60 (2000) 722–727.

[19] E. Ruoslahti, RGD and other recognition sequences for integrins, Annu. Rev. Cell Dev. Biol. 12 (1996) 697–715.

[20] E. Koivunen, B. Wang, E. Ruoslahti, Phage libraries displaying cyclic peptides with different ring sizes: ligand specificities of the RGD-directed integrins, Biotechnology (NY) 13 (1995) 265–270.

[21] N. Maeda, Y. Takeuchi, M. Takada, Y. Sadzuka, Y. Namba, N. Oku, Anti-neovascular therapy by use of tumor neovasculature-targeted long-circulating liposome, J. Control. Release 100 (2004) 41–52.

[22] F. Pastorino, C. Brignole, D. Marimpietri, M. Cilli, C. Gambini, D. Ribatti, R. Longhi, T.M. Allen, A. Corti, M. Ponzoni, Vascular damage and anti-angiogenic effects of tumor vessel-targeted liposomal chemotherapy, Cancer Res. 63 (2003) 7400–7409.

[23] N. Oku, K. Doi, Y. Namba, S. Okada, Therapeutic effect of adriamycin encapsulated in long-circulating liposomes on Meth-A-sarcoma-bearing mice, Int. J. Cancer 58 (1994) 415–419.

[24] J.M. Saul, A.V. Annapragada, R.V. Bellamkonda, A dual-ligand approach for enhancing targeting selectivity of therapeutic nanocarriers, J. Control. Release 114 (2006) 277–287.

[25] K. Shimizu, T. Asai, C. Fuse, Y. Sadzuka, T. Sonobe, K. Ogino, T. Taki, T. Tanaka, N. Oku, Applicability of anti-neovascular therapy to drug-resistant tumor: Suppression of drug-resistant P388 tumor growth with neovessel-targeted liposomal adriamycin, Int. J. Pharm. 296 (2005) 133–141.

Evaluation of O-[^{18}F]fluoromethyl-D-tyrosine as a radiotracer for tumor imaging with positron emission tomography [☆]

Takeo Urakami[a], Koichi Sakai[b], Tomohiro Asai[a], Dai Fukumoto[b], Hideo Tsukada[b], Naoto Oku[a],*

[a]*Department of Medical Biochemistry and Global COE, University of Shizuoka Graduate School of Pharmaceutical Sciences,
Yada, Suruga-ku, Shizuoka 422-8526, Japan*
[b]*PET Center, Central Research Laboratory, Hamamatsu Photonics K.K., Hamamatsu 434-8601, Japan*

Abstract

O-[^{18}F]Fluoromethyl-D-tyrosine (D-[^{18}F]FMT) has been reported as a potential tumor-detecting agent for positron emission tomography (PET). However, the reason why D-[^{18}F]FMT is better than L-[^{18}F]FMT is unclear. To clarify this point, we examined the mechanism of their transport and their suitability for tumor detection. The stereo-selective uptake and release of enantiomerically pure D- and L-[^{18}F]FMT by rat C6 glioma cells and human cervix adenocarcinoma HeLa cells were examined. The results of a competitive inhibition study using various amino acids and a selective inhibitor for transport system L suggested that D-[^{18}F]FMT, as well as L-[^{18}F]FMT, was transported via system L, the large neutral amino acid transporter, possibly via LAT1. The in vivo distribution of both [^{18}F]FMT and [^{18}F]FDG in tumor-bearing mice and rats was imaged with a high-resolution small-animal PET system. In vivo PET imaging of D-[^{18}F]FMT in mouse xenograft and rat allograft tumor models showed high contrast with a low background, especially in the abdominal and brain region. The results of our in vitro and in vivo studies indicate that L-[^{18}F]FMT and D-[^{18}F]FMT are specifically taken up by tumor cells via system L. D-[^{18}F]FMT, however, provides a better tumor-to-background contrast with a tumor/background (contralateral region) ratio of 2.741 vs. 1.878 with the L-isomer, whose difference appears to be caused by a difference in the influence of extracellular amino acids on the uptake and excretion of these two isomers in various organs. Therefore, D-[^{18}F]FMT would be a more powerful tool as a tumor-detecting agent for PET, especially for the imaging of a brain cancer and an abdominal cancer.
© 2009 Published by Elsevier Inc.

Keywords: O-[^{18}F]Fluoromethyl tyrosine; D-isomer; Positron emission tomography (PET); System L transporter; Tumor imaging

1. Introduction

[^{18}F]FDG is the most widely used tracer for tumor detection with PET imaging. However, several limitations with [^{18}F]FDG have been reported, such as a high uptake in normal brain and heart and in inflammatory tissues [1]. In contrast, the accumulation of positron emitter-labeled amino

acids was assumed to reflect enhanced amino acid transport, metabolism and protein synthesis. Therefore, these amino acid tracers have been used for detecting tumors especially those in the brain.

Positron emitter-labeled amino acids and their derivatives, such as 1-[^{11}C]methionine [2], methyl-[^{11}C]methionine [2,3], 1-[^{11}C]tyrosine [4], 1-[^{11}C]leucine [5], 1-[^{11}C]phenylalanine [6], 4-[^{18}F]fluoro-phenylalanine [7], [^{18}F]fluoro-L-tyrosine [8], have been proposed as PET imaging agents. Among these positron emitter-labeled amino acids, [^{11}C]methionine is widely used for tumor imaging with PET. Recently, several amino acid analogs, namely, O-[^{11}C]methyl-L-tyrosine [9], O-[^{18}F]fluoromethyl-L-tyrosine (L-[^{18}F]FMT) [9], O-[^{18}F]fluoroethyl-L-tyrosine [10,11], O-[^{18}F]fluoropropyl-L-tyrosine [12,13], [^{11}C]ethyo-nine [14] and [^{11}C]propionine [14], were synthesized and evaluated as PET imaging agents. These amino acid

analogues showed relatively low accumulation in normal peripheral tissue (low tissue-to-blood ratio), rapid blood clearance and a rather high amount of label remaining in tumor tissues (high tumor-to-blood ratio).

In contrast to L-isomers of amino acids, D-isomers are considered to behave as unnatural amino acids, like the amino acid analogs mentioned above. In previous reports in the 1980s, in vivo and in vitro experiments using ^{14}C-labeled D-amino acids revealed that the accumulation of D-isomers was higher than that of L-isomers in tumor cells [15,16]. At that time, the potential of D-isomers of amino acids as nuclear imaging agents was mentioned [15–17]. However, the precise mechanism responsible for the higher accumulation of the D-isomers has remained unclear. Recently, the biological functions of D-isomers in the central nervous system [18], developmental biology [19] and some pathological conditions [20,21] were reported, although the precise behavior of D-isomers still remains to be clarified [22].

Amino acid transport across the plasma membrane is mediated via amino acid transporters located on the membrane. Among the amino acid transport systems, system L, a Na$^+$-independent neutral amino acid transporter system, is the major route for providing cells with large neutral amino acids including branched or aromatic amino acids [23]. Recently, system L amino acid transporters 1 and 2 (LAT1 and LAT2) were isolated, and their characteristics were evaluated [24–26]. LAT1 was shown to be strongly expressed in malignant tumors [27,28] and also expressed in some normal organs such as brain, spleen, placenta and testis [29]. In contrast, the distribution of LAT2 mRNA is ubiquitous [30,31]. We previously reported that the D-isomer of O-[^{18}F]fluoromethyl-L-tyrosine (D-[^{18}F]FMT) was highly accumulated in tumor tissue [32,33], although the accumulation of D-[^{18}F]FMT in normal tissues, e.g., brain, kidney and pancreas, was low as was the whole-body background. However, the molecular mechanism of D-[^{18}F]FMT uptake in tumor tissue was not addressed at that time. Since the presence of amino acids in plasma would affect the uptake of this tracer into tissues, the concentrations of amino acids in plasma, in normal and tumor tissues, and in the microenvironment of tumor cells must be considered [34].

In this study, the characteristics and utility of the D-isomer of an artificial amino acid labeled with ^{18}F positron emitter were evaluated; and the behavior of L-[^{18}F]FMT and D-[^{18}F]FMT both in vitro and in vivo was examined.

2. Materials and methods

2.1. Materials

L-Alanine, L-glycine, L-phenylalanine, L-serine, D-leucine and L-leucine were purchased from Wako Pure Chemical Co. Ltd. (Osaka, Japan). 2-Aminobicyclo-(2,2,1)-heptane-2-carboxylic acid (BCH) was obtained from Sigma-Aldrich Japan (Tokyo, Japan). All other reagents were of analytical grade.

2.2. Synthesis of labeled compound

Positron-emitting ^{18}F was produced by ^{18}O(p,n)^{18}F nuclear reaction using the cyclotron (HM-18; Sumitomo Heavy Industry, Japan) at Hamamatsu Photonics PET Center. L- and D-Isomers of [^{18}F]FMT were synthesized by reacting [^{18}F]fluoro-methyl bromide with the corresponding L- and D-tyrosine according to a previous report [32,33]. Enantiomeric purity was analyzed on a CHIOBIOTIC T column (4.6×250 mm; Tokyo Kasei Kogyo). The elution solution was ethanol/water (1:1), and the flow rate was 1 ml/min. The production of [^{18}F]FDG was performed according to the method reported previously [35]. Specific activities of D-[^{18}F]FMT, L-[^{18}F]FMT and [^{18}F]FDG were 115±10, 126±12 and 144±21 GBq/μmol, respectively; and radiochemical purities were 99.6±0.4%, 99.8±0.3% and 100.0±0.0%, respectively.

2.3. Cell culture

C6 glioma cells (ATCC, Rockville, MD, USA) and HeLa cells (RIKEN, Tsukuba, Japan) were grown in Dulbecco's Modified Eagle's Medium (DMEM, Wako) supplemented with 10% fetal bovine serum (Japan Bioserum, Hiroshima, Japan) and appropriate concentrations of antibiotics (100 U/ml penicillin and 100 μg/ml streptomycin). The cells were maintained in plastic culture flasks at 37°C in a humidified atmosphere containing 5% CO$_2$ and kept as monolayers.

2.4. Measurement of uptake by cells in culture

Rat C6 glioma cells and HeLa cells were plated in 24-well culture plates (Corning Japan, Tokyo, Japan) at a density of 2×10^5 cells per well and cultured for 24 h. After the growth medium had been removed, the cells were washed twice with Hank's balanced salt solution (HBSS; 136.6 mM NaCl, 5.4 mM KCl, 4.2 mM NaHCO$_3$, 1 mM CaCl$_2$, 0.5 mM MgCl$_2$, 0.44 mM KH$_2$PO$_4$ and 0.41 mM MgSO$_4$) and kept in HBSS for 30 min at 37°C to deplete any residual nutrients from the growth medium. Then the HBSS was discarded, and the uptake assay was started by adding a trace amount of D- or L-isomer of [^{18}F]FMT/HBSS (1–3 MBq/ml) to the cultures. After incubation for the selected time period (2, 5, 10, 30 and 60 min), the uptake of labeled compounds was terminated by removing the medium. After the cells had been washed twice with 1 ml of ice-chilled Dulbecco's phosphate-buffered saline (PBS), the cells were lysed in 400 μl of cell lysis solution (0.1 M NaOH, 2% Triton X-100). The radioactivity in the cell lysates was measured by a γ-counter (Aloka ARC-2000). More than three independent experiments, each done in triplicate, were performed.

2.5. Tracer release from cultured cells

Experiments were performed using 24-well culture plates. HeLa cells (2×10^5 cells/well) were incubated with D- or L-isomer of [^{18}F]FMT (1-3 MBq/ml) in HBSS for 30 min at 37°C. Then, the cells were washed three times with HBSS, and all supernatants were discarded. Release experiments were started by the addition of 1 ml HBSS. The supernatant

was collected at each time point from each well, and cells in the well were washed twice with ice-chilled PBS very quickly. Then the cells were lysed with 400 μl of cell lysis solution (0.1 M NaOH, 2% Triton X-100), and the radio-activity in the cell lysates was measured by a γ-counter. More than three independent experiments, each done in triplicate, were performed.

2.6. Reverse transcriptase–polymerase chain reaction

Total RNAs were isolated from C6 glioma and HeLa cells by using an RNA purification kit (QIAshredder and RNeasy kit, QIAGEN KK, Tokyo, JAPAN) in accordance with the manufacturer's instructions. Then, the first-strand cDNAs were prepared with a Superscript First-strand Synthesis system (Invitrogen Japan KK, Tokyo, Japan) and oligo(dT) primer, and used as a template for polymerase chain reaction (PCR) amplification. The PCR amplification was performed with Ex Taq (Takara Bio, Inc., Ohtu, Japan) according to the following protocol [27]: 94°C for 5 min, followed by 25 cycles of 94°C for 30 s, 60°C for 30 s and 72°C for 1 min and a final extension step of 72°C for 10 min. The following primer pairs were used for PCR amplification: 5′-CAATGGTGTGGCCATCATG-3′ and 5′-GATGCATCCCCTTGTCCTAT-3′ for rat LAT1, 5′-TCATTGGCTCCGGAATCTTC-3′ and 5′-ATGCA TTCTTTGGCTCCAGC-3′ for rat LAT2, 5′-TCACAGGCT-TATCCAAGGAG-3′ and 5′-TACAATGTCAGCCTGAG-GAG-3′ for rat 4F2hc, 5′-TTCATCGCA- GTACATCG-TGG-3′ and 5′-CCCAGGTGATAGTTCCCGAA-3′ for human LAT1, 5′-AGCCCTGAAGAAAGAGATCG-3′ and 5′-TGCATATCTGTACAATCCCC-3′ for human LAT2, 5′-TCGATTACCTGAGCTCTCTG-3′ and 5′-GGGATTTTG-TATGCTCCCCA-3′ for human 4F2hc and 5′-TGACGGGGTCACCCACACTGTGCCCATCTA-3′ and 5′-CTAGAAGCATTTGCGGTGGACGATGGAGGG-3′ for human and rat β-actin.

2.7. Animals

All animals were maintained and handled in accordance with the recommendations of the National Institutes of Health and the Animal Facility Guidelines of the University of Shizuoka.

The mice bearing tumors were prepared as reported previously [32]. Briefly, female BALB/cA Jcl-nu mice (7 weeks old) were inoculated subcutaneously with 5×10^6 HeLa cells, maintained for 2 weeks after the transplantation and used for experiments at 9 weeks of age.

Male Fischer rats (9 weeks old) were obtained from Japan SLC, Inc. The rat C6 brain tumor model was prepared as reported elsewhere with a minor modification [36]. Rats were anesthetized with chloral hydrate and individually placed in a stereotaxic apparatus. C6 glioma cells (2×10^5 cells/10 μl of DMEM containing 1% gelatin) were injected at a rate of 1.0 μl/ min into the left hippocampus of the rat (−4.7 mm posterior to bregma, −3.9 mm lateral to the midline suture and −6.2 mm from the dura) via a 28-gauge stainless tube. Eleven days after tumor implantation, the rats were used for PET studies.

2.8. Whole-body imaging of tumor-bearing mice and rats

The distribution pattern of each radiolabeled compound in the rats was determined with a small-animal PET system (Clairvivo PET, Shimadzu, Kyoto, Japan). Animals were anesthetized by an intraperitoneal injection of chloral hydrate at 400 mg/kg, followed by continuous infusion of the anesthetic at 100 mg/kg per hour through a cannula placed into a tail vein. Anesthetized rats were fixed on an animal holder. Each [18F]-radiolabeled compound at a dose of 7 MBq was injected intravenously into each rat via a tail vein. The data were obtained with a list mode data acquisition every 1 s for 60 min. Reconstruction was made by 3D-DRAMA (two iterations, γ=0.1) with resolution modeling. After the PET analysis, the rat brains were excised and sliced into eight coronal slices of 2-mm thickness (four slices anterior to and four slices posterior to the optical chiasm) with a brain slicer (Muromachi Kikai, Co. Ltd, Tokyo, Japan). The distribution of [18F]FMT or [18F]FDG in each brain slice was determined by autoradiography after exposure to an imaging plate for approximately 1 h. The autoradiograms of the brain slices were obtained by using a Bio-imaging analyzer BAS1500 and analyzed by Image Gauge V3.45 (Fuji Photo Film, Co. Ltd, Tokyo, Japan).

3. Results

3.1. Uptake and release of [18F]FMT in vitro

The enantiomeric purity of each isomer was determined by the enantiomeric analytic HPLC as reported previously [33]. The results showed the enantiomeric purity of each isomer to be more than 98%.

At first, we examined the transport of the D- and L-isomers of [18F]FMT in rat C6 glioma cells and HeLa cells. The uptake of D- and L-isomers of [18F]FMT into these cells was measured at selected time points up to 30 min. As a result, the uptake rate of the L-isomer was significantly higher than that of the D-isomer in both C6 glioma and HeLa cells (Fig. 1). The uptake was not saturated at least up to 60 min (data not shown).

Then, the release of the D- and L-isomers from HeLa cells in the presence or absence of 100 μM L-leucine was examined. As shown in Fig. 2A, the release of the D-isomer under the amino acid-free condition in HBSS was slower than that of L-isomer. On the other hand, the release rate of both L-[18F]FMT and D-[18F]FMT was accelerated in the presence of L-leucine (Fig. 2B). These uptake and release experimental results on [18F]FMT indicate that the amino acid transport activity of the D-isomer was lower than that of the L-isomer in both C6 glioma and HeLa cells in vitro. Then, we further examined the selectivity of the transporter by performing inhibition experiments in C6 glioma cells. The uptake of D- and L-isomers of [18F]FMT was strongly inhibited in the presence of 1 mM L-isomers of methionine, phenylalanine and tyrosine (Fig. 3A). The uptake was also
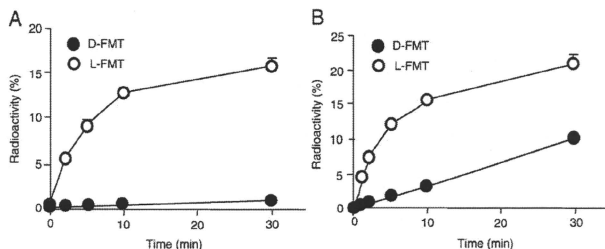
Fig. 1. Time-dependent uptake of D- and L-isomers of [^{18}F]FMT by C6 glioma and HeLa cells. The C6 glioma (A) and HeLa (B) cells were incubated for 1, 2, 5, 10 or 30 min in uptake solution containing 1–3 MBq of D- or L-isomers of [^{18}F]FMT. The relative radioactivity (as a percentage of the total dose) at each point is indicated as the mean±S.D. More than three independent experiments, each done in triplicate, were performed.

inhibited by BCH, a selective inhibitor of the system L amino acid transporter. However, the uptake was not inhibited by L-glycine. These inhibition patterns in the presence of amino acids for uptake of D- and L-isomers of [^{18}F]FMT were essentially the same, suggesting that both D- and L-isomers of [^{18}F]FMT were taken up by the same transporter, namely, the system L amino acid transporter.

Since the activity of the system L amino acid transporter is reported to be independent of extracellular sodium ions [24,25], we next examined the sodium ion dependency of the D- and L-[^{18}F]FMT transport. A sodium ion-free condition was obtained by substitution of sodium chloride with choline chloride, as reported previously [25]. Fig. 3B shows the sodium ion-independent uptake of both D- and L-isomers. These results support the idea that both D- and L- isomers of [^{18}F]FMT are transported by system L amino acid transporters.

Next, the effect of the competitive inhibition of the system L amino acid transporter on the uptake of D- or L-isomer of [^{18}F]FMT was examined. D-[^{18}F]FMT or L-[^{18}F]FMT was loaded into HeLa cells in the presence of the various

concentrations of BCH, a selective inhibitor of system L (Fig. 4A). The uptake of both D- and L-isomers of [^{18}F]FMT was inhibited by BCH in a dose- dependent manner. Furthermore, the inhibitory effect of various concentrations of natural amino acids, i.e., D- and L-leucine, on isomer uptake was examined. Both D- and L-leucine inhibited the uptake of [^{18}F]FMT; however, L-[^{18}F]FMT uptake was decreased more at a low concentration of the extracellular amino acids (Fig. 4B and C) than the D-isomer. These results suggest that the transport of L-[^{18}F]FMT was more affected in the presence of either L-leucine or D-leucine than that of the D-isomer in vitro and that this might also be the case in vivo.

System L amino acid transporter proteins LAT1 and LAT2 were isolated previously. LAT1 and LAT2 require an additional single-membrane-spanning protein heavy chain of the 4F2 antigen (4F2hc) for their functional expression in the plasma membrane. LAT1 and 4F2hc or LAT2 and 4F2hc form a heterodimeric complex via a disulfide bond. So we examined the mRNA expression of the system L amino acid transporters in C6 glioma and HeLa cells. In the reverse
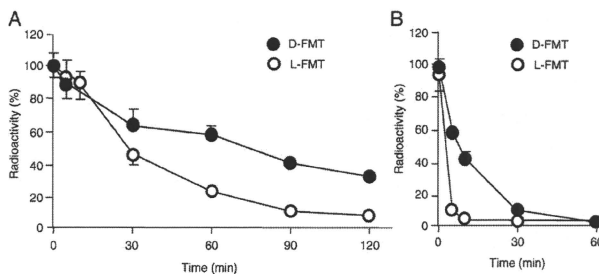

Fig. 2. Release of D- and L-isomers of [^{18}F]FMT preloaded in HeLa cells. The release of preloaded [^{18}F]FMT from HeLa cells was examined. The cells preloaded with D- or L-isomers of [^{18}F]FMT were incubated in the absence (A) or presence (B) of 100 μM L-leucine. The relative radioactivities that remained in the cells were determined to obtain the release rate of [^{18}F]FMT. Each point indicates the mean±S.D. More than three independent experiments, each carried out in triplicate, were performed.
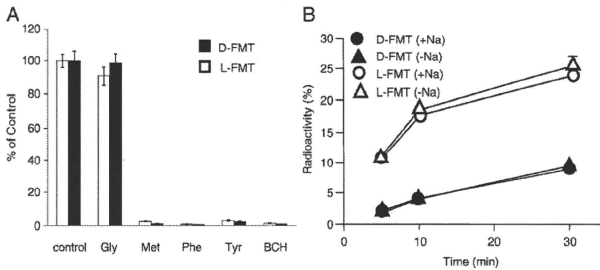
Fig. 3. Uptake of D- and L-isomers of [^{18}F]FMT by C6 glioma cells in the presence of amino acids, inhibitors and Na$^+$ ions. (A) C6 glioma cells were incubated with D- or L-isomer of [^{18}F]FMT in the uptake solution containing L-glycine, L-methionine, L-phenylalanine, L-tyrosine or BCH (100 μM for each). The relative radioactivity in the cells was determined. (B) C6 glioma cells were incubated with D- or L-isomer of [^{18}F]FMT in the uptake solution in the presence (circles) or absence (triangles) of Na$^+$ ions. The relative radioactivity of cells was determined. Data are presented as the relative mean uptake±S.D.

transcriptase–PCR (RT-PCR) analysis, the PCR products for LAT1 and their associating protein 4F2hc, but not the LAT2 product, were detected when RNA from the rat C6 glioma and HeLa cell cultures was used (Fig. 5).

3.2. Tumor PET imaging with [^{18}F]FMT

Noninvasive real-time imaging with a small-animal PET provides distribution data consistent with those obtained from tissue dissection assays. Mice xenografted with HeLa

cells were prepared and examined by PET. Data were acquired from mice administered D-[^{18}F]FMT, L-[^{18}F]FMT or [^{18}F]FDG (Fig. 6). The mouse injected with D-[^{18}F]FMT showed the clearest difference in tracer intensity between the tumor (right leg) and the normal tissue (left leg) compared with the mice given the other tracers. The accumulation of D-[^{18}F]FMT in the tumor tissue was not different from that of L-[^{18}F]FMT. The standard uptake value (SUV) of the former was 1.336; and that of the latter, 1.642. However,
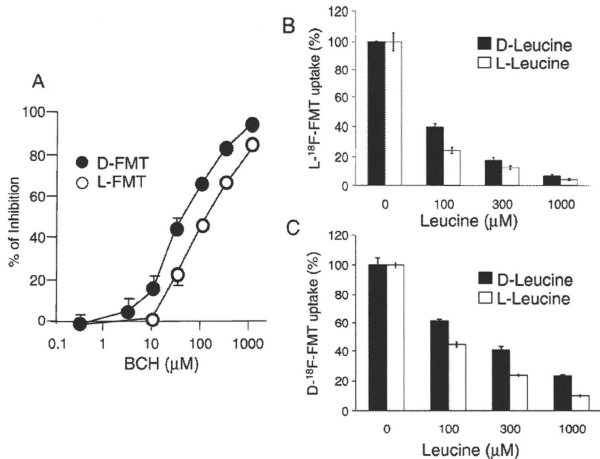

Fig. 4. BCH- and L- or D-leucine-mediated inhibition of D- or L-[^{18}F]FMT uptake by HeLa cells. The uptake of D- (open circle) or L-isomer (closed circle) of [^{18}F] FMT was measured for 5 min in the presence of various concentrations of BCH (A). The stereo-selective inhibitory effect of leucine on the uptake of L-[^{18}F]FMT (B) and D-[^{18}F]FMT (C) into HeLa cells was examined in the presence of 0, 100, 300 and 1000 μM L- or D-leucine. The graph shows the % radioactivity of the control (without leucine). Bars indicate the mean±S.D.
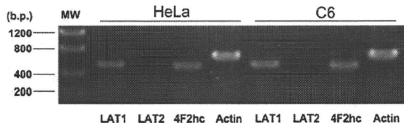
Fig. 5. RT-PCR detection of LAT1, LAT2 and 4F2hc mRNAs in HeLa and C6 cells. First-strand cDNAs prepared from cultured C6 glioma and HeLa cells were used as templates for PCR amplification. The PCR products were subjected to agarose gel electrophoresis and visualized with ethidium bromide.

there was far less radioactivity in the normal tissue in the case of the image obtained with the D-isomer of [^{18}F]FMT: SUVs for D-[^{18}F]FMT and L-[^{18}F]FMT were 0.488 and 0.874, respectively.

Finally, the in vivo tumor imaging in the brain tumor model was examined. Data were displayed as the image of
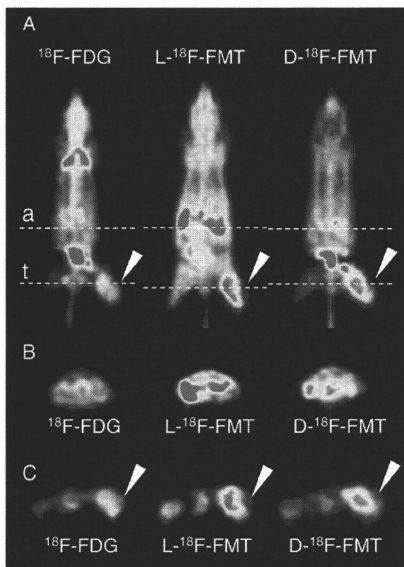

Fig. 6. Small-animal PET images of [^{18}F]FDG, L-[^{18}F]FMT and D-[^{18}F]FMT in tumor-bearing mice. Mice were inoculated with HeLa cells, and radiolabeled compounds were injected intravenously for the PET imaging. Coronal plane images (A), axial plane images of the abdominal region (B) and axial plane images of tumor implanted region (C) after injection of [^{18}F] FDG, L-[^{18}F]FMT or D-[^{18}F]FMT are shown. The broken lines "a" and "t" indicate the position of the axial plane image of the abdominal region (B) and the tumor region (C), respectively. The arrowhead points to the tumor. The typical images from multiple independent experiments (n>3) are shown.
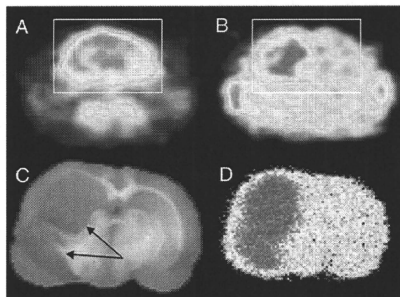

Fig. 7. Small-animal PET images of D-[^{18}F]FMT and [^{18}F]FDG in a brain tumor-bearing rat. PET imaging of [^{18}F]FDG (A) and D-[^{18}F]FMT (B) was performed in the same rat bearing a C6 glioma brain tumor. The brain area in the PET image is indicated by the square. After the PET study with D-[^{18}F] FMT, brain slices were prepared to confirm the location of the tumor (arrows, C) and to detect the radioactivity of D-[^{18}F]FMT in the brain by autoradiography (D). Note that images in (C) and (D) are expanded beyond the square region (brain). Five separate experiments were performed, and similar results were obtained. Data typical of one of them are shown here.

the D-isomer of [^{18}F]FMT in comparison with that of [^{18}F] FDG in the rat C6 glioma orthotopic brain tumor model, as shown in Fig. 7. In this model of brain tumor, [^{18}F]FDG could not detect the tumor specifically due to the high background in the normal brain tissue (Fig. 7A). In contrast, D-[^{18}F]FMT showed a lower accumulation in the normal region of the brain (Fig. 7B), and thus the tumor region in the brain was imaged. (Comment in Fig. 7C and D).

4. Discussion

In the present study, we investigated the properties of ^{18}F-labeled D- and L-isomers of artificial amino acid FMT in relation to their transport activity in cultured C6 glioma and HeLa cells. In addition, the specificity of amino acid transporters engaged in the transport of D- and L-isomers of [^{18}F]FMT was examined.

Concerning ^{18}F-PET studies, positron emitter-labeled diagnostic drugs possess very high specific radioactivity: specific activities of D-[^{18}F]FMT, L-[^{18}F]FMT and [^{18}F]FDG in the present study were 115±10, 126±12 and 144±21 GBq/μmol, respectively. Therefore, the experiment was performed by using amino acids at the tracer level concentration. The uptake study on the D- and L- isomers of [^{18}F]FMT in C6 glioma and HeLa cells in HBSS suggested that the incorporation was mediated by a stereo-selective amino acid transporter, since the L-isomer was incorporated much faster than the D-isomer (Fig. 1).

The release of D- and L-isomers of [^{18}F]FMT was examined by use of HeLa cells preloaded with each isomer

of [^{18}F]FMT. The release of D-[^{18}F]FMT from the cells was slower than that of L-isomer (Fig. 2A). This result is consistent with the uptake data. Since intra/extracellular amino acid exchange was reported as a feature of the system L amino acid transport system [25], the presence of extracellular amino acid would enhance the release of intracellular [^{18}F]FMT in system L. In fact, the release of both D- and L-isomers of [^{18}F]FMT was up-regulated by extracellular 100 μM L-leucine, a typical substrate of system L (Fig. 2B). The physiological concentration of leucine in human plasma is approx. 100 μM, as reported previously [34,37]. Considering the situation of tumor cells in the living body, there would be plenty of extracellular amino acids in the plasma; and they would have an effect on both the uptake and release of amino acid-related PET tracers.

To clarify the involvement of the transport system in [^{18}F]FMT uptake, we examined the inhibition of uptake of the D- or L-isomer of [^{18}F]FMT by the L-isomer of various amino acids and by a system L selective inhibitor, BCH, in C6 glioma cells. BCH is an amino acid-related compound that competitively inhibits both LAT1 and LAT2. Large neutral amino acids (L-methionine, L-phenylalanine and L-tyrosine) and BCH inhibited the uptake of both D- and L-isomers of [^{18}F]FMT completely; but L-glycine, a small neutral amino acid, did not inhibit it at all (Fig. 3A). Furthermore, system L is known to be a Na$^+$-independent amino acid transporter [24,25]. To make clear the character of the transport system, we examined the Na$^+$ dependency of uptake of D- and L-isomers of [^{18}F]FMT. The uptake of D- and L-isomers of [^{18}F]FMT was not affected by the presence of Na$^+$ ions (Fig. 3B).

Moreover, the RT-PCR experiment done to determine the expression of the major system L transporters LAT1 and LAT2 and their functional associated protein 4F2hc indicated that both C6 glioma and HeLa cells expressed LAT1 and 4F2hc mRNA but not LAT2 (Fig. 5). These results suggest that the major transporter of system L in C6 glioma and HeLa cells was LAT1. Based on these results taken together, we conclude that both D- and L-isomers of [^{18}F]FMT were transported via LAT1 in C6 glioma and HeLa cells. However, the involvement of other transport systems in the actual or in the other tumors is possible.

The dose-dependent inhibitory effect of BCH on D- or L-isomer of [^{18}F]FMT uptake (Fig. 4A) indicated that there was little difference in the IC$_{50}$ value between D- and L-isomers. Comparison of the inhibitory effect of D and L isomers of leucine on the uptake of FMT showed that the uptake of L-[^{18}F]FMT was inhibited at low concentrations of these isomers (Fig. 4B and C). Under physiological conditions, the concentration of amino acids transported via the system L in the plasma is far higher than 100 μM [34]. These data suggest that both D- and L-isomers of [^{18}F]FMT would be competitively transported by system L transporters.

To develop tumor-detecting agents, it is important to have not only higher accumulation in the tumor but also a lower background. This tumor/normal tissue ratio of accumulation highly influences the contrast obtained. Previous reports

indicated that the accumulation of [^{18}F]FMT in tumors evaluated by SUV did not differ between D- and L-isomers during a 60-min post administration, but showed that the tumor/blood ratio was significantly different [32,33]. In the present study, we also observed that the SUV of L-isomer was quite similar to that of the D-isomer in tumor tissue, although the latter was only about one-half of the former in normal tissue. At the time point of 60 min, the tumor/blood ratio of D-[^{18}F]FMT was twice as high as that of the L-isomer [32,33]. A previous report suggested that the L-configuration of amino acids is required for the optimal active reabsorption in the renal tubules [38]. D-Isomer of amino acids might be less reabsorbed and consequently more excreted than that of L-isomer. Therefore, as a result, the contrast imaging of tumors was achieved by D-[^{18}F]FMT.

For in vivo evaluation of D-[^{18}F]FMT, we adopted a mouse xenotransplantation model using human tumor cells as a small-animal model for predicting the accumulation of tumor tracer candidates in human tumor cells. [^{18}F]FDG was accumulated not only in the tumor but also in the brain and in the heart. There was not a large difference between the accumulations of L- and D-[^{18}F]FMT in the tumor. However, the accumulation of the tracer in the normal tissue around the tumor, abdominal, chest and brain region was considerably lower with D-[^{18}F]FMT than with L-[^{18}F]FMT. These results suggest that D-[^{18}F]FMT is more suitable for a tumor-detecting agent.

Finally, we evaluated tumor imaging with D-[^{18}F]FMT by using a rat allograft orthotopic brain tumor model. A current report suggests that there is a significant difference in some pathological and pharmacological features between orthotopic tumor models and ectopic tumor models in rodents [39]. Because the conditions of tissues and the bloodstream around the tumor are important for the evaluation of tumor-imaging agents, we selected a rat orthotopic tumor model. With rats bearing C6 glioma transplanted into their left middle brain, we conducted a small-animal PET experiment using D-[^{18}F]FMT. The positron emitter-labeled tracer was injected via a tail vein. The brain tumor, which could not be detected by [^{18}F]FDG PET due to high background, was imaged by D-[^{18}F]FMT. The region of the tumor and autoradiographic image visualized on tumor slices well correlated with the D-[^{18}F]FMT accumulation imaged by PET. These results suggest that D-[^{18}F]FMT might be a useful tracer for tumor detection.

5. Conclusions

This study demonstrated that the artificial large neutral amino acid FMT was accumulated into tumor cells via amino acid transporters. The LAT1 system L transporter was suggested to be the transporter, at least in C6 glioma and HeLa cells. The uptake, release and exchange of L-[^{18}F]FMT were more affected by a physiological concentration of extracellular amino acids than those of the D-isomer. D-[^{18}F]